Journal of Computational Physics 519 (2024) 113378

Contents lists available at ScienceDirect

Journal of Computational Physics

journal homepage: www.elsevier.com/locate/jcp

A vertically non-uniform temperature approach for the friction term computation in depth-averaged viscoplastic lava flows

J. Ortega-Moya [a,*], S. Martínez-Aranda [a], J. Fernández-Pato [b], P. García-Navarro [a]

[a] *Fluid Dynamic Technologies - I3A, University of Zaragoza, Zaragoza, Spain*
[b] *Estación Experimental Aula Dei, CSIC, Zaragoza, Spain*

ARTICLE INFO

Keywords:
Viscoplastic shallow flows
Bingham model
Liquefied lava flows
Depth-averaged non-Newtonian models
Temperature exchange
Finite volume methods

ABSTRACT

Recently, depth-averaged shallow flow models have been adapted to modelling liquefied lava flows, generally characterized by a marked temperature-dependent non-Newtonian rheology. Modelling these complex flows requires to include the effects of the depth-averaged temperature gradients in the governing equations. The most significant term to correctly predict the lava mobility is the flow resistance term, which is widely estimated using the linear viscoplastic Bingham model. This non-Newtonian model allows to relate the bed shear stress to the depth-averaged lava flow features by means of a cubic equation with analytical solution when assuming a uniform temperature distribution along the vertical profile. Nevertheless, the lava temperature is non-uniform along the vertical due to the heat transfer at the bottom and the free surface, and hence the classical cubic Bingham model is not valid anymore. In this work, a depth-averaged shallow flow model is adapted for realistic lava flows considering influence of the non-uniform vertical temperature profile in the non-Newtonian resistance. This requires to modify the rheological viscoplastic models for ensuring the coupling between flow dynamics and temperature evolution. Three non-uniform temperature vertical distributions are considered: linear, piece-wise and diffusion profiles. Synthetic tests are used to show the influence of the temperature vertical profile on the numerical results. Furthermore, laboratory experimental data are used to validate this novel viscoplastic resistance formulation and to show that the calibration of its parameters is possible.

1. Introduction

Depth-averaged shallow flow models are widely used for the numerical simulation of hydraulic/hydrological free surface processes, such as river and coastal flows, runoff generation in steep slopes, fast floods, tsunami waves, highly erosive sediment-laden flows, muddy slurries and debris flows [1–5]. Nevertheless, the depth-averaged approach has also been applied to generalized gravity-driven free-surface flows with complex behaviour, such as viscous and viscoplastic flows [6] or oil spills over land [7]. Recently, special attention has been dedicated to modelling lava flows, which are characterized by a temperature-dependent rheology [8,9]. Usually, modelling these complex flows requires to include the effects of the depth-averaged temperature gradients in the governing equations [10,11]. Although the lava density slightly depends on the temperature, the main effect of the temperature variation is the change of the rheological properties which control the flow mobility.

---

[*] Corresponding author.
E-mail address: 810298@unizar.es (J. Ortega-Moya).

https://doi.org/10.1016/j.jcp.2024.113378
Received 4 December 2023; Received in revised form 30 July 2024; Accepted 24 August 2024

Despite the complexity of characterizing lava rheology [12], the most widespread model to address the morphological bulk behaviour of lava flows is the linear viscoplastic Bingham model [13,14]. This simplified constitutive model is derived from the generalized Herschel-Bulkley model for non-linear viscoplastic fluids [15] considering that the shear stress τ evolves with the strain rate, i.e. the rate of deformation $\dot{\gamma}$, depending on two temperature-dependent parameters: the yield strength τ_y for the motion initialization and the Bingham viscosity μ accounting for the fluid consistency. Usually, the dependence of these rheological parameters on the temperature is addressed using exponential relations [16]. Since the flow structure along the vertical coordinate is lost in depth-averaged models, the suitable application of the Bingham constitutive model to estimate the flow resistance term in free-surface viscoplastic models requires to express the boundary shear stress at the bottom interface of the moving layer τ_b as a function of the bulk flow features, i.e. the flow depth h and the depth-averaged velocity components $\overline{u}$ and $\overline{v}$. The widespread solution consists of assuming that the transient flow structure is the same as that of a steady viscoplastic flow running over an infinite uniform slope. This assumption is often referred to as the infinite landslide [17,18], since it was initially formulated for landslides with complex rheology, and leads to the classical cubic Bingham closure for viscoplastic free-surface flows [19–21].

The derivation of the cubic Bingham model was made under the hypothesis that the yield strength remains constant along the vertical direction [19] and hence it also implies that the temperature is constant along the lava flow column [16]. However, the temperature along the vertical coordinate is likely to show a non-uniform profile due to the heat transfer (temperature exchange) at the bottom and free surface interfaces. The heat exchange term at the upper and bottom interfaces can be included in shallow flows and numerous empirical and analytical models have been proposed. The simplest heat exchange model only includes natural convection and radiation at the surface and heat conduction at the bottom [22]. On the other hand, the most complex temperature transfer models take into account various mechanisms such as natural and forced convection, radiation, rain and latent heat of phase change [23]. In general, experimental evidence [24,25] indicates that the main mechanism of heat transfer throughout the free surface and the bottom interfaces of lava flows is convection whereas, inside the lava layer, temperature transfer occurs mainly by conduction.

Concerning the numerical modelling of the lava flow mobility using the viscoplastic Bingham model, the main drawback of considering a non-uniform temperature profile along the vertical coordinate is that the rheological parameters, i.e. yield strength and viscosity, change along the flow column. Hence, the widespread cubic closure relationship for the viscoplastic flow resistance is not valid anymore. In the last decade, the most remarkable efforts to include the effects of the vertical variation of the fluid driven-properties on the depth-averaged viscoplastic dynamics have been developed for the pore-fluid pressure in landslides and debris flows. Different approaches have been developed to model the vertical dissipation of pore pressure, from considering a time-dependent linear non-hydrostatic pressure profile [26,27] to deriving more complex quadratic shape functions for the non-hydrostatic component based on the dilation of the solid phase [28,29]. Furthermore, [17,30] proposed a diffusion equation for pore pressure that was solved using a finite difference vertical mesh, allowing to model changes of boundary conditions at the bottom surface. Although all these works were focused on the vertical variation of the pore pressure in sediment-laden flows, the proposed approach can be recalled to analyze the effects of vertical temperature distribution on the dynamics of thermal-driven viscoplastic flows.

The main goal of this work is to derive a new depth-averaged shallow flow model [9] for realistic lava flows considering the influence of the non-uniform vertical temperature profile in the non-Newtonian resistance at the bottom surface. This requires to modify the rheological viscoplastic model for ensuring the coupling between flow dynamics and temperature evolution. The dependence of the bottom shear stress on the depth-averaged flow features should be reconstructed, achieving a novel correlation between the flow mobility and the temperature gradients. The outline of the text is as follows: first, in Section 2, the depth-averaged governing equations are recalled with a particular emphasis on the generation of a non-Newtonian resistance model under different rheological conditions. The consequences of assuming a variable temperature profile along the fluidized lava column are highlighted and a new resistance model is proposed in that situation. Then, the numerical method used to solve the governing equations is summarized in Section 4. Numerical test cases are included in Section 5. Synthetic tests are used to show the influence of the assumed temperature profile on the numerical results, whereas laboratory experimental data are used to validate our formulation and to show that a calibration of its parameters is possible. Finally, the main conclusions are drawn in Section 6.

2. Governing equations for viscoplastic thermal-driven surface flows

The general depth-averaged shallow flow equations can be derived by integrating the Navier-Stokes system along the z-coordinate from the bottom surface z_b to the free surface $z_s = z_b + h$, where h denotes the fluid depth. The mass-conservation law reads:

$$\frac{\partial(\overline{\rho}h)}{\partial t} + \frac{\partial}{\partial x}(\overline{\rho}h\overline{u}) + \frac{\partial}{\partial y}(\overline{\rho}h\overline{v}) = 0, \tag{1}$$

where $\overline{\rho}$ is the depth-averaged density whereas $\overline{u}$ and $\overline{v}$ are the components of the depth-averaged velocities along the $x-$ and $y-$coordinates, respectively. The momentum equations along the $x-$ and $y-$ directions take the form:

$$\frac{\partial(\overline{\rho}h\overline{u})}{\partial t} + \frac{\partial}{\partial x}\left(\overline{\rho}h\overline{u}^2 + \frac{1}{2}g\overline{\rho}h^2\right) + \frac{\partial}{\partial y}\left(\overline{\rho}h\overline{uv}\right) = -g\overline{\rho}h\frac{\partial z_b}{\partial x} - \tau_{bx} \tag{2}$$

$$\frac{\partial(\overline{\rho}h\overline{v})}{\partial t} + \frac{\partial}{\partial x}\left(\overline{\rho}h\overline{uv}\right) + \frac{\partial}{\partial y}\left(\overline{\rho}h\overline{v}^2 + \frac{1}{2}g\overline{\rho}h^2\right) = -g\overline{\rho}h\frac{\partial z_b}{\partial y} - \tau_{by} \tag{3}$$

being g the gravity acceleration and (τ_{bx}, τ_{by}) the components of the basal resistance vector $\boldsymbol{\tau_b}$. Note that the effects of the density variation along the flow depth are neglected in equations (2)-(3), in order to simplify the formulation of the convective momentum fluxes and the hydrostatic pressure terms [15]. Finally, the depth-averaged temperature equation is considered:

$$\frac{\partial(\overline{\rho}h\overline{T})}{\partial t} + \frac{\partial(\overline{\rho}h\overline{T}\overline{u})}{\partial x} + \frac{\partial(\overline{\rho}h\overline{T}\overline{v})}{\partial y} = \frac{\dot{Q}}{c_P}, \tag{4}$$

where $\overline{T}$ is the depth-averaged temperature, $\dot{Q}$ the heat flux throughout the upper and bottom interfaces and c_P the specific heat of the fluidized material. At the free surface, the heat transfer with the air is mainly governed by convection and radiation exchange fluxes, $\dot{Q}_{conv}$ and $\dot{Q}_{rad}$ respectively. For the convection mechanism, a simple law is assumed:

$$\dot{Q}_{conv} = h_c(T_s - T_{air}) \tag{5}$$

where h_c is the convection coefficient, T_{air} denotes the air temperature and T_s is the temperature of the flow at the free surface. For the radiation mechanism, the Stefan-Boltzmann Law is applied:

$$\dot{Q}_{rad} = \epsilon\sigma(\overline{T}^4 - T_{air}^4) \tag{6}$$

where ϵ is the surface emissivity and $\sigma = 5.67 \cdot 10^{-8}\, W/(m^2K^{-4})$ is the Stefan-Boltzmann constant. Although the value of ϵ is still object of debate, experimental measurements in [24] suggest a value of 0.74, whilst other authors prefer a value near 0.90-0.95 ([23]).

When working with depth-averaged equations, the influence of the viscous stress tensor arises in the momentum equation in the form of the shear stress vector at the bottom surface, i.e. the basal resistance vector $\boldsymbol{\tau_b}$, which can be expressed as:

$$\boldsymbol{\tau_b} = (\tau_{bx}, \tau_{by}) = \tau_b\, \mathbf{n_u}, \tag{7}$$

where τ_b is the basal shear stress and $\mathbf{n_u} = (n_{ux}, n_{uy}) = (\overline{u}, \overline{v})/\sqrt{\overline{u}^2 + \overline{v}^2}$ is the flow unit vector defined by the depth-averaged velocity. It is essential to find a closure relation to evaluate the shear resistance at the bottom as a function of the depth-averaged flow variables. This relation will depend on the rheological behaviour of the fluidized material.

2.1. *Depth-averaged approach for the viscoplastic basal resistance*

In order to find a generalized closure relation for the basal shear stress τ_b, we consider the general expression for the viscous stress tensor:

$$\boldsymbol{\tau} = \Phi(I_{2D})\mathbf{D}, \tag{8}$$

where $\mathbf{D} \equiv D_{ij} = \frac{1}{2}(\partial_j u_i + \partial_i u_j)$ is the strain rate tensor and Φ is a scalar function of $I_{2D} = \frac{1}{2}\,\mathrm{Tr}\left(\mathbf{D}^2\right)$. In the case of the generalized Herschel-Bulkley viscoplastic model, this function can be expressed [15] as:

$$\Phi(I_{2D}) = \frac{\tau_0}{\sqrt{I_{2D}}} + 2K_\Phi(4I_{2D})^{\frac{m-1}{2}}, \tag{9}$$

where τ_0, K_Φ and m are parameters to be determined depending on the rheological behaviour of the fluid.

The infinite landslide method [17] assumes that the flow structure corresponds to that of a simple shear steady flow, where the velocity along the flow column is almost horizontal and only depends on the vertical position: $\mathbf{u} = (u, v, 0) = \left(\mathrm{U}(z)\, n_{ux}, \mathrm{U}(z)\, n_{uy}, 0\right)$, being $\mathrm{U}(z) = \sqrt{u^2 + v^2}$ the magnitude of the horizontal velocity, the viscoplastic stress tensor can be expressed as:

$$\boldsymbol{\tau} = \begin{pmatrix} 0 & 0 & \tau(z)\, n_{ux} \\ 0 & 0 & \tau(z)\, n_{uy} \\ \tau(z)\, n_{ux} & \tau(z)\, n_{uy} & 0 \end{pmatrix}, \tag{10}$$

where $z \in [0, h]$ denotes the vertical coordinate above the bottom surface and $\tau(z)$ is the shear stress along the flow column:

$$\tau(z) = \Phi(I_{2D})\, \frac{1}{2}\, \frac{d\mathrm{U}}{dz}, \tag{11}$$

$$I_{2D} = \frac{1}{4}\left(\frac{d\mathrm{U}}{dz}\right)^2. \tag{12}$$

Then, a simplified linear shear stress profile is assumed along the flow column as follows:

$$\tau(z) = \tau_b \left(1 - \frac{z}{h}\right), \tag{13}$$

where $\tau_b = \tau(z = 0)$ is the value of the resistance at the bottom surface. It is noteworthy that the linear shear stress profile only fully holds in the case of vertically uniform flow density. If the density weakly depends on another fluid driven-property, such as temperature, equation (13) should result in a good approximation to the stress profile under the infinite flow hypothesis [17]. This assumption is commonly used to derive relationships for the basal shear stress in depth-averaged models and will be implicit in the following viscoplastic models.

The shear stress (13) is integrated along the flow column to obtain the velocity profile $\mathrm{U}(z\,|\,h,\tau_b)$, which depends on the basal shear stress and the flow depth. The velocity profile is integrated again to derive an expression for the flow discharge involving the depth-averaged velocity magnitude $\overline{\mathrm{U}}(h,\tau_b)$, allowing to compute the basal shear stress τ_b from the shallow flow features as:

$$\overline{\mathrm{U}}(h,\tau_b)=\frac{1}{h}\int\limits_0^h \mathrm{U}(z\,|\,h,\tau_b)\,dz \qquad \Longrightarrow \qquad \tau_b=\mathcal{F}(h,\overline{\mathrm{U}}). \tag{14}$$

This procedure is the method by which the most common viscoplastic resistance relations for shallow flow equations have been derived [15], such as the classical Bingham model. It is worth mentioning that these depth-averaged friction models should depend on the fluid driven-properties, i.e. the temperature T for lava flows, not only through the variation of the rheological parameters in (9) but also through the density variations. However, the density dependence is assumed negligible due to the selection of a simplified linear shear stress profile along the flow column.

3. Viscoplastic resistance models

In this section we introduce the procedure to develop a functional relationship between the bed shear stress and the depth-averaged flow features for non-uniform temperature distributions along the vertical coordinate. First, the basic case of uniform temperature in the flow column is considered. Then, different non-uniform vertical temperature profiles are addressed.

3.1. Classic Bingham model

A common model to describe viscoplastic thermally-controlled fluids, such as lava, is the linear Bingham model. This is a particular case of the Herschel-Bulkley model (9) using $\tau_0=\tau_y$, $K_\Phi=\mu$ and behaviour index $m=1$, leading to:

$$\tau(z)=\tau_y+\mu\frac{d\mathrm{U}}{dz}. \tag{15}$$

Here, τ_y represents a yield stress which is the minimum stress necessary to deform the fluid and μ is the dynamic viscosity coefficient. Equation (15) is expressed assuming that $\frac{dU}{dz}>0$ and hence $\tau(z)>\tau_y$. The classical Bingham-type models assume that the yield strength and the viscosity are uniform along the vertical coordinate, i.e. that the fluid temperature is homogeneous along the flow column. When $\tau_b\le\tau_y$, then $\overline{\mathrm{U}}=0$, otherwise, if $\tau_b>\tau_y$, this hypothesis allows to express the variation of the velocity along the vertical coordinate $z\in[0,h]$ as:

$$\frac{d\mathrm{U}}{dz}=\begin{cases}0 & \text{if } z_0<z<h\\ \frac{1}{\mu}\left[\tau_b\left(1-\frac{z}{h}\right)-\tau_y\right] & \text{if } 0<z<z_0\end{cases} \tag{16}$$

where $z_0=h\left(1-\frac{\tau_y}{\tau_b}\right)$ denotes the shear layer depth, i.e. the height where $\tau(z)$ becomes smaller than the yield stress τ_y. Hence, in the plug region $z\in[z_0,h]$ above the shear layer, the strain rate becomes null and the velocity is uniform. Therefore, the velocity profile $\mathrm{U}(z)$ is straightforward:

$$\mathrm{U}(z)=\begin{cases}\frac{\tau_b h}{2\mu}\left(1-\frac{\tau_y}{\tau_b}\right)^2 & \text{if } z_0<z<h\\ \frac{\tau_b-\tau_y}{\mu}z-\frac{\tau_b}{2h\mu}z^2 & \text{if } 0<z<z_0\end{cases} \tag{17}$$

and the flow discharge can be expressed as:

$$h\overline{\mathrm{U}}=\int\limits_0^h \mathrm{U}(z)\,dz=\frac{h^2}{2\mu}\left(\frac{2}{3}\tau_b-\tau_y+\frac{\tau_y^3}{3\tau_b^2}\right), \tag{18}$$

from where we can finally find a cubic closure relation for the basal resistance $\tau_b(h,\overline{\mathrm{U}})$:

$$\left(\frac{\tau_y}{\tau_b}\right)^3-\left(3+\frac{6\mu\overline{\mathrm{U}}}{\tau_y h}\right)\frac{\tau_y}{\tau_b}+2=0 \tag{19}$$

which is valid for $\tau_b\ge\tau_y$ and is usually rewritten as:

$$\frac{\overline{\mathrm{U}}}{h}=\begin{cases}0 & \text{if} \quad \tau_b<\tau_y\\ \frac{1}{3}\left(\frac{\tau_y^3}{2\mu\tau_b^2}-\frac{3\tau_y}{2\mu}+\frac{\tau_b}{\mu}\right) & \text{if} \quad \tau_b\ge\tau_y\end{cases} \tag{20}$$

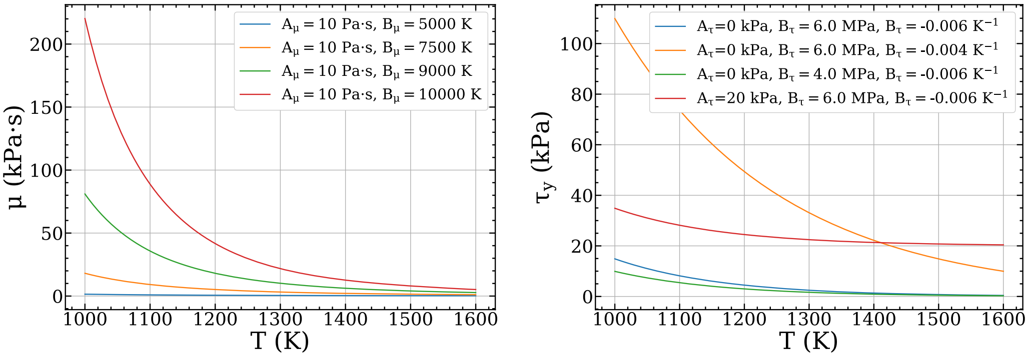

(a) Viscosity relation given by (23).

(b) Yield stress relation given by (24).

Fig. 1. Dependence of the fluid rheological properties on the temperature.

It is worth noting that the derivation of the classical Bingham cubic closure (19) is made assuming that the yield strength τ_y and the viscosity μ are uniform along the flow column, as well as the flow density ρ. This equation will be used to calculate the theoretical uniform temperature profile for comparative purposes. Furthermore, some authors computed the solution for the bed shear stress τ_b in the cubic equation (19) using iterative methods, such as Newton-Raphson, or deploying approximate quadratic equations to the original Bingham in order to improve the robustness of the bed resistance estimation [20,31,32].

The Bingham relation (20) can be reordered in dimensionless terms as:

$$\frac{\mu\overline{\mathrm{U}}}{\tau_y h} = \begin{cases} 0 & \text{if} \quad \tau_b/\tau_y < 1 \\ \frac{1}{3}\left(\frac{\tau_y^2}{2\tau_b^2} - \frac{3}{2} + \frac{\tau_b}{\tau_y}\right) & \text{if} \quad \tau_b/\tau_y \geq 1 \end{cases} \tag{21}$$

which can be simplified for cases where $\tau_b/\tau_y > 3/2$ to the linear dimensionless expression:

$$\frac{\mu\overline{\mathrm{U}}}{\tau_y h} = \begin{cases} 0 & \text{if} \quad \tau_b/\tau_y < 3/2 \\ \frac{1}{3}\left(\frac{\tau_b}{\tau_y} - \frac{3}{2}\right) & \text{if} \quad \tau_b/\tau_y \geq 3/2 \end{cases} \tag{22}$$

The expression (22) could be considered as a good approximation to the classical cubic Bingham stress curve for values $\tau_b/\tau_y \geq 2$, allowing an easier computation of the flow resistance in these cases. For the particular pure-viscous case, the yield strength is null ($\tau_y = 0$) and the simple Newtonian fluid $\tau_b = 3\mu\overline{\mathrm{U}}/h$ is found. Furthermore, if the viscous component is null, i.e. pure-cohesive fluids, the velocity profile cannot be obtained using the infinite landslide hypothesis unless an additional assumption is made. In this sense, viscosity regularizes the problem [17], allowing to derive the vertical velocity profile.

3.2. *Variable coefficient models*

In the case of a temperature-dependent Bingham fluid, the hypothesis of uniform rheological properties along the vertical coordinate is only satisfied if the fluid temperature is also uniform. However, the heat exchange of the flow with the bottom layer and the upper atmosphere leads to a non-uniform temperature profile in the flow column and hence the classical Bingham closure is not valid anymore.

3.2.1. *Temperature-dependent viscoplastic coefficients*

To find novel closure relation for the basal shear resistance, first, it is necessary to formulate the variability of viscosity and yield stress with the fluid temperature. In this text we will consider a few models, but the procedure is easily extended to others. For the temperature-dependent viscosity $\mu(T)$, the Andrade model [33,34,9] reads:

$$\mu(T) = A_\mu \exp\left(B_\mu/T\right), \tag{23}$$

being A_μ $[Pa \cdot s]$ and B_μ $[{}^\circ K]$ rheological fitting parameters, whereas the temperature-dependent yield stress $\tau_y(T)$ is expressed using the following exponential relation [35,9]:

$$\tau_y(T) = A_\tau + B_\tau \exp\left(C_\tau T\right), \tag{24}$$

where A_τ $[Pa]$, B_τ $[Pa]$, C_τ $[1/{}^\circ K]$ are fitting parameters. Fig. 1 depicts the variation of the fluid viscosity and yield strength on the temperature, depending on the rheological parameters considered.

When the temperature profile $T(z)$ is non-uniform, the shear stress relation (15) obtained is more complicated, as it includes dependencies on the $z-$coordinate in the rheological parameters:

$$\tau\big(T(z),z\big) = \tau_y\big(T(z)\big) + \mu\big(T(z)\big)\,\frac{d\mathrm{U}}{dz} \tag{25}$$

Introducing the expressions for $\tau_y(T)$ and $\mu(T)$, the strain rate along the flow column is expressed as:

$$\frac{d\mathrm{U}}{dz} = \begin{cases} 0 & \text{if } \tau(z) < \tau_y\big(T(z)\big) \\ \dfrac{\tau_b\left(1-\frac{z}{h}\right) - \left[A_\tau + B_\tau \exp\left(C_\tau T(z)\right)\right]}{A_\mu \exp\left(B_\mu / T(z)\right)} & \text{if } \tau(z) \geq \tau_y\big(T(z)\big) \end{cases} \tag{26}$$

The assumption of temperature-dependent rheological parameters causes that a clear differentiation of the shear layer and the plug zone along the flow column is not straightforward. Therefore, the vertical flow structure depends on the local dynamics features and the temperature profile. The integration of the strain rate profile (26) is generally non-elementary and becomes impossible to complete the process as originally stated for the classical Bingham hypothesis.

Even considering that the temperature profile $T(z)$ can be fully determined from the flow depth h and the depth-averaged temperature $\overline{T}$, proposing a functional dependency for $\tau_b = \mathcal{F}(\overline{T}, h, \overline{\mathrm{U}})$ may be a complex process. Therefore, a dimensional analysis is performed in order to simplify the problem by applying the Vaschy-Buckingham Π Theorem [36]. First, we define the normalized variables:

$$z' = \frac{z}{h} \qquad \mathrm{U}' = \frac{\mathrm{U}}{\overline{\mathrm{U}}} \qquad T' = \frac{T}{T_h} \tag{27}$$

and we consider that dimensionless temperature distribution $T'(z')$ is known and fully characterized by a set of dimensionless parameters $\mathcal{S}$, which include the univocal shape-relation between the depth-averaged temperature $\overline{T}$ and the reference maximum temperature T_h. This reference temperature is considered constant and must be defined depending on the type of vertical temperature profile selected.

The Vaschy-Buckingham Π Theorem states that, considering n physical parameters involved in a problem, they can be combined in $(n-r)$ dimensionless variables $\Pi_1, \ldots \Pi_{n-r}$, where r is the rank of the dimensional matrix of exponents in the base of fundamental variables involved. In this case, there exist $n = 10$ dimensional parameters $\left\{A_\mu,\, B_\mu,\, A_\tau,\, B_\tau,\, C_\tau,\, \overline{T},\, T_h,\, \overline{\mathrm{U}},\, h,\, \tau_b\right\}$, while $r = 4$ dimensions $\left\{\text{length, time, mass, temperature}\right\}$ are involved. Therefore, we can simplify the dependencies to six dimensionless parameters, $\Pi_1, \Pi_2, \ldots, \Pi_6$, defined as:

$$\Pi_1 = \frac{\tau_b}{B_\tau} \qquad \Pi_2 = \frac{A_\mu\,\overline{\mathrm{U}}}{B_\tau\, h} \qquad \Pi_3 = \frac{\overline{T}}{T_h} \tag{28}$$

$$\Pi_4 = \frac{A_\tau}{B_\tau} \qquad \Pi_5 = C_\tau\, T_h \qquad \Pi_6 = \frac{B_\mu}{T_h} \tag{29}$$

and the strain rate along the vertical coordinate (26) can be rewritten in dimensionless form as:

$$\frac{d\mathrm{U}'}{dz'} = \frac{\Pi_1\,(1-z') - \Pi_4 - \exp\left(\Pi_5\, T'\right)}{\Pi_2\, \exp\left(\Pi_6 / T'\right)} \tag{30}$$

Hence the normalized velocity derivative (30) can be integrated along the vertical coordinate and the Π theorem ensures the existence of the relationship:

$$\Pi_2 = f(\Pi_1, \Pi_4, \Pi_5, \Pi_6, \mathcal{S}) \tag{31}$$

where $\mathcal{S}$ includes the dimensionless shape parameter Π_3 for the normalized temperature vertical distribution $T'(z')$. However, once the rheological parameter A_μ, B_μ, A_τ, B_τ, C_τ of the fluid are fixed and the reference maximum temperature T_h is defined, the numbers Π_4, Π_5, and Π_6 become constant. Consequently, the dependency reduces to an equation of the form:

$$\Pi_2 = \tilde{f}(\Pi_1, \mathcal{S}) \tag{32}$$

and only the set $\left\{\tau_b,\, h,\, \overline{T}\right\}$ must be specified. Therefore, setting constant dimensionless numbers $\left\{\Pi_4,\, \Pi_5,\, \Pi_6\right\}$, the dimensionless derivative (30) can be integrated twice to find the averaged velocity $\overline{\mathrm{U}}$. If this integration is repeated for a wide range of $\left\{\tau_b,\, h,\, \overline{T}\right\}$, the functional relationship $\tilde{f}$ in (32) can be found. Accordingly, in this work, the following procedure for approximating the bed shear stress τ_b is proposed:

1. A set of discrete values for h, $\overline{T}$ and τ_b is considered, taking values in some intervals of interest:

$$\left\{\overline{T}^1, \overline{T}^2, \ldots, \overline{T}^{N_T}\right\} \subset \left[\overline{T}_{\min}, \overline{T}_{\max}\right]$$
$$\left\{h^1, h^2, \ldots, h^{N_h}\right\} \subset \left(0, h_{\max}\right)\big]$$
$$\left\{\tau_b^1, \tau_b^2, \ldots, \tau_b^{N_\tau}\right\} \subset \left[\tau_y, \tau_{b\max}\right]$$

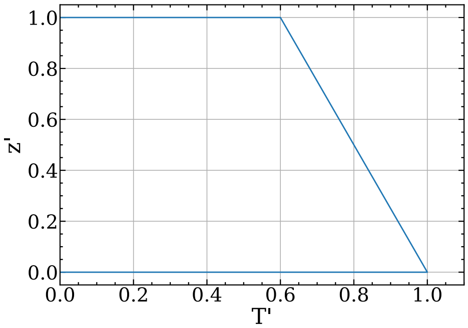

Fig. 2. Normalized linear temperature profile with $T_h = 300$ K and $\overline{T} = 240$ K.

Table 1
Two different sets of parameters to describe fluids with different rheological parameter.

	A_τ (Pa)	B_τ (Pa)	C_τ (K^{-1})	A_μ (Pa· s)	B_μ (K)
Fluid 1	10	2000	-0.02	0.08	1200
Fluid 2	0	$5.6 \cdot 10^6$	$-5.8 \cdot 10^{-3}$	1.77	9500

2. The velocity profile $\mathrm{U}(z)$ is numerically integrated from (26) for each combination of parameters. Therefore, $N_T \times N_h \times N_\tau$ different numerical velocity profiles $\mathrm{U}(z \,|\, \overline{T}, h, \tau_b)$ are computed.
3. Each velocity profile is integrated numerically in order to obtain the depth-averaged velocity $\overline{\mathrm{U}}^{ijk} = \overline{\mathrm{U}}(\overline{T}^i, h^j, \tau_b^k)$. The result of this step is a set of tuples $\{(\overline{T}^i, h^j, \tau_b^k, \overline{\mathrm{U}}^{ijk})\}$ with $i = 1, 2, ..., N_T$, $j = 1, 2, ..., N_h$ and $k = 1, 2, ..., N_\tau$.
4. A functional dependency $\tau_b = \mathcal{F}(\overline{T}, h, \overline{\mathrm{U}})$ is proposed and fitted to the discrete values previously computed.

3.2.2. Linear temperature model

First, the proposed procedure is illustrated in the simplest non-uniform temperature profile corresponding to a linear temperature distribution along the flow column:

$$T(z) = T_h - 2(T_h - \overline{T})\frac{z}{h} \tag{33}$$

where the reference maximum temperature T_h is constant and set at the bed surface $z = 0$ (see Fig. 2). This is a special case of generalized functional relationship (32) where the shape $\mathcal{S}$ of the normalized temperature distribution $T'(z')$ is fully described by the dimensionless parameter $\Pi_3 = \overline{T}/T_h$.

Following the procedure reported in the above section, the velocity profile integration is done for a wide set of values of $\{\tau_b, h, \overline{T}\}$. The results show that, under the condition that τ_b is considerably larger than τ_y, i.e. $\tau_b \gg \tau_y$, the dimensionless number Π_2 depends almost linearly on Π_1 with a slope and axis-intersection point being functions of Π_3. Hence, it can be expressed as:

$$\Pi_2 = \tilde{f}_1(\Pi_3)\,\Pi_1 + \tilde{f}_2(\Pi_3). \tag{34}$$

As a final step, for simplicity, the fixed parameters that form the dimensionless numbers are absorbed into the functions $\tilde{f}_1$ and $\tilde{f}_2$, resulting in a dimensional relationship:

$$\frac{\overline{\mathrm{U}}}{h} = \begin{cases} 0 & \text{if } \tau_b \le \tau_{b0} \\ f_1(\overline{T})\,\tau_b + f_2(\overline{T}) & \text{if } \tau_b > \tau_{b0} \end{cases} \tag{35}$$

where $\tau_{b0} = \dfrac{-f_2(\overline{T})}{f_1(\overline{T})}$ is an effective yield stress.

This linear dependence can be observed in the examples shown in Fig. 3 for two different parameter sets representing two fluids with differentiated rheology (see Table 1). To generate this graph, 20 values of both the basal shear stress τ_b and the flow depth h were employed, along with 40 values of depth-averaged temperature $\overline{T}$, resulting in almost $1.6 \cdot 10^4$ integrals relations. Not all temperature values are represented, since the lines would not be distinguishable, but all values of h are plotted. So each point on the Fig. 3 actually consists of 20 overlapping points corresponding to the values of h for a certain stress and temperature. This confirms the conclusion derived from the Π theorem: we can eliminate one parameter because $\overline{\mathrm{U}}$ and h are not independent, i.e. only their quotient is representative.

It is worth noting the equivalence between the generalized expression (35) for non-uniform linear temperature distribution and the simplified relation for the uniform temperature profile (22). Both formulas state that the relation between the bed shear stress τ_b and the depth-averaged velocity $\overline{\mathrm{U}}$ can be estimated by a linearized approximation (see Fig. 3). This similarity partly explains

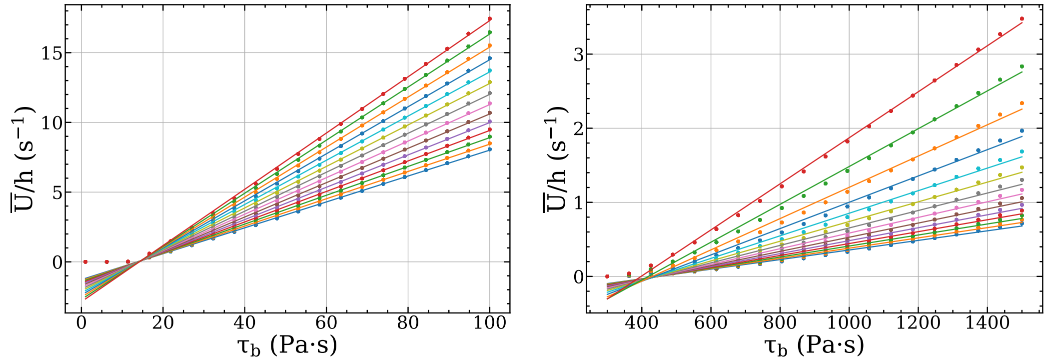

(a) Fluid 1, T_h=400 K (b) Fluid 2, T_h=1500 K

Fig. 3. Linear dependency of $\overline{\mathrm{U}}/h$ with τ_b for the fluid rheology in Table 1. Each line corresponds to a different value of averaged temperature.

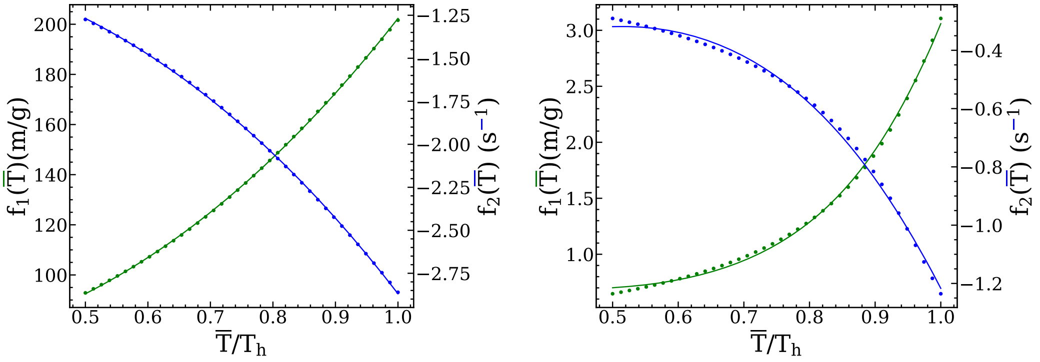

(a) Fluid 1 (b) Fluid 2

Fig. 4. Fitting of the temperature-dependent slope and axis-interception functions, $f_1(\overline{T})$ and $f_2(\overline{T})$, for the rheological parameters shown in Table 1.

the structure of the generalized functional relationship (35). As particular case of (35), the Newtonian relation is the trivial choice, since it holds a pure linear dependence of the shear stress with the fluid viscosity. For a classical Bingham fluid, the first term on the right-hand side in (20) becomes negligible compared to the second one for $\tau_b \gg \tau_y$, and τ_y and μ are functions of $\overline{T}$, hence demonstrating the proposed approximated relationship.

Thus, the problem has been reduced to the linear fitting of successive lines at constant temperature and the approximation of two functions of a single variable, $f_1(\overline{T})$ and $f_2(\overline{T})$. It is noteworthy that the shape of these functions varies depending on the parameter values used, but a good fit can be easily found. In particular, it has been observed that functions that work relatively well for a wide range of different parameters are:

$$f_1(\overline{T}) = A_1 + B_1\overline{T}^{n_1} \tag{36}$$

$$f_2(\overline{T}) = A_2\overline{T}^3 + B_2\overline{T}^2 + C_2 \tag{37}$$

where A_1, B_1, n_1, A_2, B_2, and C_2 are fitting constants. The fitting of $f_1(\overline{T})$ and $f_2(\overline{T})$ for the fluids considered in Table 1 are shown in Fig. 4. The significance of this result is that, if more complex temperature profiles are tested, the relationships obtained here hold approximately, as it is shown in the next sections.

It is worth noting that the relationships used in this work for the viscosity and the yield strength, (23) and (24) respectively, can be replaced by other models with an arbitrary number of constant parameters. These additional parameters will be absorbed into constant dimensionless numbers in the same way that occurred with A_μ, B_μ, A_τ, $B_\tau$and C_τ. However, for the dimensional analysis to be valid, the temperature profile needs to be unequivocally described by the flow depth h, the depth-average temperature $\overline{T}$ and an arbitrary number of constants with temperature units, which would have an analogous treatment to that of T_h. This gives some freedom to create more realistic temperature distributions. Furthermore, the functions $f_1(\overline{T})$ and $f_2(\overline{T})$, in (36) and (37) respectively, do not have any physical background and they should be modified if required by the model parameters, the rheology laws and the temperature profile chosen.

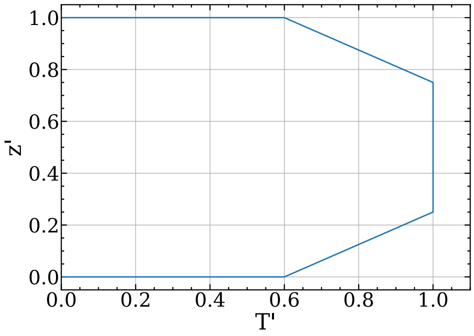

Fig. 5. Normalized piece-wise temperature profile with $n = 4$, $T_h = 300$ K and $\overline{T} = 270$ K.

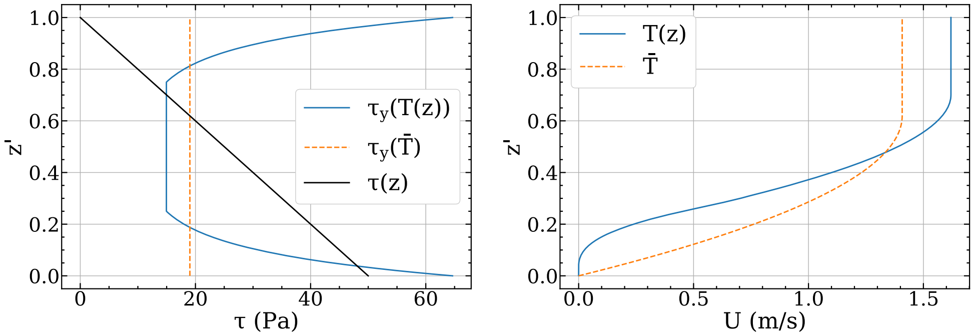

(a) Yield stress (b) Velocity

Fig. 6. Comparison between yield stress and velocity profiles in the case of uniform temperature and a piece-wise profile ($n = 4$, $T_h = 300$ K, $\overline{T} = 270$ K) for an arbitrary rheological configuration of parameters ($A_\tau = 10$ Pa, $B_\tau = 2000$ Pa, $C_\tau = 0.02$ K^{-1}, $A_\mu = 0.08$ Pa· s and $B_\mu = 1200$ K) with a basal stress $\tau_b = 50$ Pa.

3.2.3. Piece-wise temperature model

The natural extension of the linear temperature profile is the piece-wise linear function. A heat transfer will be assumed at the bottom and free surfaces so that they are colder, with corresponding temperatures $T_b = T_s$, whereas the maximum reference temperature T_h is constant and set at the center region of the fluid column. Also, we also assumed that the temperature gradient takes place in a layer of width $\delta_T = h/n$. Hence, the temperature profile can be expressed as:

$$T(z) = \begin{cases} T_s + (T_h - T_s)\frac{h-z}{\delta_T} & \text{if} \quad (h-\delta_T) < z \le h \\ T_h & \text{if} \quad \delta_T < z \le (h-\delta_T) \\ T_b + (T_h - T_b)\frac{z}{\delta_T} & \text{if} \quad 0 < z \le \delta_T \end{cases} \tag{38}$$

This model is similar to the one considered in [6] and we will take $n = 4$ assuming that conduction as the unique heat transfer mechanism [8]. Both surface temperatures $T_b = T_s$ can be written in terms of the depth-averaged temperature as $T_b = T_s = n\overline{T} - T_h(n-1)$, and hence the shape $\mathcal{S}$ of the normalized temperature profile $T'(z')$ is fully described by the dimensionless parameter $\Pi_3 = \overline{T}/T_h$. Fig. 5 shows the graphical representation of the resulting piece-wise profile.

Fig. 6-(a) represents the induced shear stress $\tau(z)$ on the flow column and yield strength $\tau_y(z)$ for uniform and piece-wise temperature distributions along the vertical direction. An important difference is observed between the uniform temperature and the piece-wise temperature profile. While the former shows an unique intersection point, separating the shear layer from the plug, the latter depicts two intersection points between the stress profile $\tau(z)$ and the yield stress profile $\tau_y(z)$. Hence, the velocity under the lower intersection point is zero, whereas above the second intersection point the velocity becomes constant (plug zone), as it is plotted in Fig. 6-(b). Interestingly, such effect is similar to the formation of two crusts of solid rock above and below the liquid lava flows due the cooling process.

At this point, we can repeat the process followed with the linear temperature profile (see Section 3.2.2) in order to fit the parameters in the functional relationships (36) and (37). Then, the shear stress τ_b is computed from the model in (35).

3.2.4. Temperature diffusion model for lava flows

A more realistic temperature profile is now proposed by using a simplified temperature diffusion model. It is noteworthy that the purpose of this approximation is not to precisely compute the temperature distribution of fluid column but to capture the main effects of its non-uniformity on the averaged flow dynamics. Therefore, the proposed model is a simplified approach to the realistic description

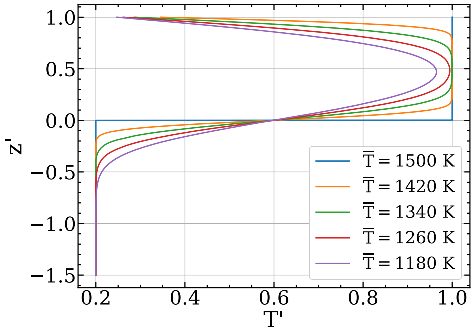

Fig. 7. Normalized diffusion temperature profiles computed solving (39) with $h = 1\,m$.

of the temperature profile in lava flows, which would have multiple layers due to crystallization, cavitation and solidification of the lava, and would also depend on time from the eruption, flow velocity and other factors.

Under the aforementioned hypothesis, it is usual to assume that the heat transference is mainly due to conduction [23,22]. The temperature distribution of the liquid lava layer ($0 < z \le h$) resting over the bedrock ($z \le 0$) is described by the following 1D heat equation problem:

$$
\begin{aligned}
&\frac{\partial T}{\partial t} = \alpha \frac{\partial^2 T}{\partial z^2} \quad -\infty < z < h, \quad t > 0\\
&\text{Boundary conditions: } \begin{cases} \left.\frac{\partial T}{\partial z}\right|_{z=h} = -\frac{1}{\kappa}(\dot{Q}_{rad} + \dot{Q}_{conv}) \\ \lim\limits_{z\to-\infty} T(z) = T_b \end{cases}\\
&\text{Initial condition:} \quad T(z) = \begin{cases} T_h & \text{if} \quad 0 > z \le h, \quad t = 0 \\ T_b & \text{if} \quad -\infty < z \le 0, \quad t = 0 \end{cases}
\end{aligned}
\tag{39}
$$

where κ is the thermal conductivity and $\alpha = \kappa/(\rho c_P)$ is the thermal diffusion coefficient, which are considered constant and equal for the solidified rock and liquid lava. In this problem the initial temperatures of the liquid lava is constant and set to the reference maximum temperature T_h, whereas the temperature of the underlying solid rock is set to $T_b < T_h$. A transmissive boundary condition is set at the free surface to model the heat transfer with the air using the convection and radiation fluxes, $\dot{Q}_{conv}$ (5) and $\dot{Q}_{rad}$ (6) respectively.

Therefore, when solving numerically equation (39), a temporal sequence of temperature profiles $\{T_{t_n}(z)\}$ is computed for discrete times $t_0 < t_1 < \cdots < t_N$, and each one has an average temperature associated (see Fig. 7). Thus, it is possible to link each time t_n with the depth-averaged value of the temperature at that time $\overline{T}$. This mapping is bijective because the mean temperature will be a monotonically decreasing function of time, i.e. the inverse mapping also exists, and hence it is possible to find a unique time $t_n = t(\overline{T})$ such that the average temperature of the computed profile is $\overline{T}$. Therefore, there exists a univocal relationship between the normalized temperature profile $T'(z')$ at each time t_n and dimensionless shape parameter $\Pi_3 = \overline{T}/T_h$, i.e. $T'_{t_n}(z') = T'(z' \,|\, \Pi_3)$.

The dimensionless form of (39) is straightforward without requiring new dimensionless Π parameters by defining a characteristic time $t_c = \rho c_P h^2/\kappa$ and normalizing time as $t' = t/t_c$ [37]. However, the convection-radiation boundary conditions imposed at the free surface leads to the solution for the temperature profile depends on the flow depth h. This requirement violates the hypothesis stated for the normalized temperature profile $T'(z')$ since additional dimensionless numbers associated to the heat transfer at the free surface are required, such as the convective Nusselt number $Nu = h\,h_c/\kappa$ [38].

To solve this issue, the case $h = 1\,m$ is chosen as reference, and other cases with $h \neq 1\,m$ are approximated by scaling the resulting temperature profiles with a variable transformation. In other words, the normalized temperature profile for a certain flow depth h and a certain depth-average temperature $\overline{T}$, referred to as $T'(z' \,|\, \Pi_3)$, is estimated from the normalized temperature distribution $\left\{T'(z')\right\}_{\Pi_3}^{h_1}$ obtained from solving (39) using $h = 1\,m$ at the time $t_n = t(\Pi_3)$ (see Fig. 7). Therefore, it is possible to repeat the same procedure as in the previous cases (see Section 3.2.2 and Section 3.2.3) in order to fit the parameters in $f_1(\overline{T})$ (36) and $f_2(\overline{T})$ (37), and to compute τ_b from the model in (35).

3.2.5. *Summary of temperature variable models*

Table 2 summarises the depth-averaged temperature range, the surface temperature T_s and the heat conduction at the bottom surface $\dot{Q}_b$ for the three proposed temperature distributions. In this sense, the use of both non-uniform piece-wise and diffusive temperature profiles may allow to derive a boundary condition for the bed surface. We apply the Fourier Law to the temperature profile in order to obtain an expression for the heat transfer with the bedrock as a function of the depth-average temperature $\overline{T}$, leading to:

$$
\dot{Q}_b = -\kappa \left.\frac{\partial T}{\partial z}\right|_{z=0}
\tag{40}
$$

Table 2
Variable temperature models: depth-averaged temperature range, surface temperature T_s and heat conduction at the bottom surface $\dot{Q}_b$.

Temperature profile	$[\overline{T}_{\min}\ ,\ \overline{T}_{\max}]$	$T_s(\overline{T})$	$\dot{Q}_b(\overline{T},h)$
Linear (33)	$\left[\frac{1}{2}(T_{air}+T_h)\ ,\ T_h\right]$	$2\overline{T}-T_h$	NO
Piece-wise (38)	$\left[\frac{1}{n}T_{air}+\frac{n-1}{n}T_h\ ,\ T_h\right]$	$n\overline{T}-(n-1)T_h$	$-\kappa\frac{n}{h}(T_h-T_b)$
Diffusion (39)	$[T_{air}\ ,\ T_h]$	Fit/Interpolation	Fit/Interpolation

It is necessary to highlight that each proposed approach, i.e. linear temperature, price-wise temperature and diffusion temperature models, has a range of validity determined by the depth-average temperature $\overline{T}$ at which the surface temperature T_s equals the air temperature T_{air}.

4. Numerical model

The system of equations formed by the mass conservation (1), the momentum conservation (2)-(3) and the transport equation for the flow temperature (4), is solved using the fist-order Finite Volume (FV) method reported by [9] for thermal-dependent viscoplastic flows. For the sake of simplicity, the over-bar notation $\langle\bar{\cdot}\rangle$ for the depth-averaged flow variables is omitted and we assume a linear dependency of the depth-averaged density on the depth-averaged temperature as:

$$\rho(T)=\rho_0+K(T-T_0), \tag{41}$$

being ρ_0 the reference depth-averaged density at the reference depth-averaged temperature T_0 and K a dependency constant. Note that this linear dependence of density on the fluid temperature is reduced in comparison with the exponential relationships provided by the rheological properties, i.e. viscosity $\mu(T)$ and yield strength $\tau_y(T)$ and hence the vertical uniform density assumption implicitly included in the momentum equations is suitable. Then, the homogeneous system is rewritten in terms of the normalized density r (42) and normalized temperature T^∇ (43):

$$r=1+\frac{K}{\rho_0}(T-T_0) \tag{42}$$

$$T^\nabla=\frac{K}{\rho_0}(T-T_0) \tag{43}$$

and the normalized density can be written as $r=1+T^\nabla$ so that the flow depth is calculated directly from the conservative variables as $h=rh-hT^\nabla$. Therefore, the homogeneous system is expressed in vector form as:

$$\frac{\partial\mathbf{U}}{\partial t}+\nabla\cdot\mathbf{E}(\mathbf{U})=\mathbf{S_b}+\mathbf{S}_\tau \tag{44}$$

where $\mathbf{U}$ is the vector of conservative variables and $\mathbf{E}=\big(\mathbf{F}(\mathbf{U}),\mathbf{G}(\mathbf{U})\big)$ denotes the conservative fluxes:

$$\mathbf{U}=\begin{pmatrix} rh \\ rhu \\ rhv \\ hT^\nabla \end{pmatrix}\qquad \mathbf{F}=\begin{pmatrix} rhu \\ rhu^2+\frac{1}{2}grh^2 \\ rhuv \\ huT^\nabla \end{pmatrix}\qquad \mathbf{G}=\begin{pmatrix} rhv \\ rhuv \\ rhv^2+\frac{1}{2}grh^2 \\ hvT^\nabla \end{pmatrix} \tag{45}$$

whereas, on the right hand side, $\mathbf{S_b}$ and $\mathbf{S}_\tau$ stand for the bed slope and basal resistance source term, respectively, expressed as:

$$\mathbf{S_b}=\begin{pmatrix} 0 \\ -grh(\partial z_b/\partial x) \\ -grh(\partial z_b/\partial y) \\ 0 \end{pmatrix}\qquad \mathbf{S}_\tau=\begin{pmatrix} 0 \\ -(\tau_b/\rho_0)\,n_{ux} \\ -(\tau_b/\rho_0)\,n_{uy} \\ 0 \end{pmatrix} \tag{46}$$

By applying the Gauss theorem, system (44) is integrated into a computational cell Ω_i as:

$$\frac{\mathrm{d}}{\mathrm{d}t}\int_{\Omega_i}\mathbf{U}\mathrm{d}\Omega+\sum_{k=1}^{NE}\left(\mathbf{E}(\mathbf{U})\cdot\mathbf{n}\right)_k l_k=\int_{\Omega_i}\mathbf{S_b}(\mathbf{U})\mathrm{d}\Omega+\int_{\Omega_i}\mathbf{S}_\tau(\mathbf{U})\mathrm{d}\Omega \tag{47}$$

where k denotes the intercell edge of length l_k, $\mathbf{n}$ is the outward unit normal vector and NE is number of neighbouring cells.

Considering an augmented fully-coupled Riemann solver for thermal-dependent compressible shallow flows [9], the numerical solution of the variables $\mathbf{U}$ at cell i for a time step $\Delta t=t^{n+1}-t^n$ is computed as:

$$\mathbf{U}_i^*=\mathbf{U}_i^n-\frac{\Delta t}{A_i}\sum_{k=1}^{NE}\mathbf{R}_k^{-1}\left[\mathbf{F}(\hat{\mathbf{U}})_k-\mathbf{H}(\hat{\mathbf{U}})_k-\mathbf{T}(\hat{\mathbf{U}})_k\right]l_k \tag{48}$$

where the superscript $\langle * \rangle$ indicate that this is not the fully updated solution, A_i is the cell area and $\mathbf{R}_k$ the rotation matrix associated to the local framework of the edge k created by the normal and tangential directions. The vector $\mathbf{F}(\hat{\mathbf{U}})$ denotes normal conservative flux vector, being $\hat{\mathbf{U}} = \mathbf{R}_k \mathbf{U}$ the rotated conservative variables, and $\mathbf{H}(\hat{\mathbf{U}})_k$ and $\mathbf{T}(\hat{\mathbf{U}})_k$ account for the bed slope and basal friction flux contributions, respectively, expressed in the local edge framework [15]. It is worth noting that, to ensure good properties, the momentum flux vectors $\mathbf{H}(\hat{\mathbf{U}})_k$ and $\mathbf{T}(\hat{\mathbf{U}})_k$ must satisfy the rotation invariant property [19].

The augmented flux at the edge k can be upwind computed using a 4-wave Riemann decomposition as

$$\mathbf{U}_i^* = \mathbf{U}_i^n - \frac{\Delta t}{A_i} \sum_{k=1}^{NE} \mathbf{R}_k^{-1} \left[\sum_{m-} (\widetilde{\lambda}_m \widetilde{\alpha}_m - \widetilde{\beta}_m - \widetilde{\sigma}_m) \widetilde{\mathbf{e}}_m \right]_k^n l_k \tag{49}$$

where $(\widetilde{\lambda}_m)_k^n$ are the wave celerities at the edge, i.e. the eigenvalues of the Jacobian matrix of the local Riemann problem (RP), $(\widetilde{\mathbf{e}}_m)_k^n$ are the eigenvectors of the RP, $(\widetilde{\alpha}_m)_k^n$ denote the wave strengths accounting for the discontinuity on the local conservative variables, $(\widetilde{\beta}_m)_k^n$ are the source strengths which include the integrated bed slope contribution and $(\widetilde{\sigma}_m)^n$ are the source strengths which include the integrated basal resistance contribution. The subscript $m-$ under the sums indicates that only the waves travelling inward the i cell are considered.

In this numerical method, the stop-moving mechanism for the flow activation is applied at each cell edge by the balance between the numerical frictionless momentum flux, including the convective and the pressure terms, i.e. $\sum_{m-} (\widetilde{\lambda}_m \widetilde{\alpha}_m - \widetilde{\beta}_m) \widetilde{\mathbf{e}}_m$, and the bed resistance contribution estimated using the selected rheological model, i.e. $\sum_{m-} \widetilde{\sigma}_m \widetilde{\mathbf{e}}_m$. This upwind method ensures the stability and non-oscillatory behaviour for highly transient flows, preserving the positivity of the flow depth, as well as the well-balanced character of the numerical solution in steady state cases, regardless the rheological formulation used to estimate bed shear stress. The detailed explanation of this upwind integration method for the bed resistance contribution and the activation of the stop-moving mechanism can be found in [19,39,40].

Once the value of the conservative variables (U) at the i cell is updated with the homogeneous transport component, intermediate values for the flow depth h_i^*, temperature T_i^* and density ρ_i^* are reconstructed as:

$$h_i^* = (rh)_i^{n+1} - (hT^{\nabla})_i^{n+1} \tag{50}$$

$$T_i^* = \frac{\rho_0}{K} \frac{(hT^{\nabla})_i^{n+1}}{(h)_i^*} + T_0 \tag{51}$$

$$\rho_i^* = \rho_0 + K(T_i^* - T_0) \tag{52}$$

Then, the non-conservative component of the heat transport equation (4) is considered as:

$$\frac{\partial (h\rho T)}{\partial t} = \frac{\dot{Q}}{C_p} \tag{53}$$

and, assuming that the flow mass remains constant despite the heat exchange through the bottom and the upper interfaces, the flow temperature at cell i is explicitly updated at time t^{n+1} as:

$$T_i^{n+1} = T_i^* + \Delta t \, \frac{\dot{Q}_i^n}{\rho_0 \, (rh)_i^n \, C_p} \tag{54}$$

Finally, the value of the remaining flow variables can be also updated with the new temperature field as

$$\begin{aligned} \rho_i^{n+1} &= \rho_0 + K(T_i^{n+1} - T_0) \\ h_i^{n+1} &= \frac{\rho_0 \, (rh)_i^{n+1}}{\rho_i^{n+1}} \\ u_i^{n+1} &= \frac{(rhu)_i^{n+1}}{(rh)_i^{n+1}}, \\ v_i^{n+1} &= \frac{(rhv)_i^{n+1}}{(rh)_i^{n+1}}. \end{aligned} \tag{55}$$

The stability condition requires that the global time step Δt is limited by the Courant-Friedrichs-Lewy (CFL) condition as:

$$\Delta t = \text{CFL} \min_k \left[\frac{\min(A_i, A_j)}{l_k \max\limits_m \left(|\widetilde{\lambda}_m|\right)_k^n} \right] \tag{56}$$

with CFL< 1 for 2D triangular cells. Therefore, the global time step is controlled by the eigenvalues $\widetilde{\lambda}_m$ of the fully-coupled Jacobian matrix, preserving stability of the numerical solution even for large temperature/density gradients. Furthermore, the upwind discretization of the source terms using the eigenvector orthonormal base avoids additional time step reductions regardless of the

Table 3
Test 1 - Heat transfer configuration.

	c_P (J/(kg· K))	T_{air} (K)	T_h (K)	h_c (W/(m^2· K))	ϵ
Case 1	-	-	450	-	-
Case 2	1	450	500	100	0,74
Case 3	1	450	500	100	0,74

Table 4
Test 2 - Rheological parameters of the simulated fluid.

Parameter	A_τ (Pa)	B_τ (Pa)	C_τ (K^{-1})	A_μ (Pa· s)	B_μ (K)
Value	0	$5.6\cdot10^{6}$	$-5.8\cdot10^{-3}$	1.77	9500

closure relationship considered for basal resistance term [15]. A comprehensive explanation of the numerical method can be found in [41,9].

5. Test cases and numerical results

5.1. Test1: 1D dambreak wave over dry flat bed

As a first synthetic test, a 1D dambreak over flat and dry bed is proposed. The reservoir initial surface level is $h_0 = 30.5$ m and the dam is located at $x_0 = 305$ m. The case is a classical benchmark test, widespread in literature [19,21], with an approximated analytical equilibrium solution that can be found when the parameters are uniform and constant [26]. The approximated analytical solution predicts a stopping position at $x_f = 1896$ m.

A comparison between three different cases is performed here: (Case 1) a fluid with constant and uniform temperature used as reference; (Case 2) a cooling fluid with a linear temperature profile; and (Case 3) a cooling fluid with a piece-wise temperature profile. For Case 1, constant density $\rho = 1835$ kg/m^3, viscosity $\mu = 100$ Pa· s, yield stress $\tau_y = 1500$ Pa and temperature $450\,K$ are assumed to approximate the analytical stopping position, following the values reported in previous works. In Case 2 and Case 3, an initially uniform temperature of $500\,K$ is stated. The heat transfer parameters used have been reported in Table 3. Their values are synthetic and selected so that the cooling process is fast.

Regarding the rheological model, the fitting parameters in (23) and (24) are selected so that the value of yield stress and viscosity at the initial time are the same as the fixed values for the constant-uniform temperature simulation: $A_\tau = 0$ Pa, $B_\tau = 30431$ Pa, $C_\tau = -0.00602$ K^{-1}, $A_\mu = 3.13$ Pa· s and $B_\mu = 1726.9$ K. Finally, in Case 2 and Case 3 the density is computed using law (41) with $\rho_0 = 1835$ kg/m^3, $K = -0.1$ kg/(m^3· K) and $T_0 = 300$ K.

Fig. 8 shows the free surface evolution until the flow stops totally, i.e. the final equilibrium state where viscoplatic shear stress remains balanced with the yield strength. A good coincidence between the stopping point predicted by the analytical approximation and the one obtained by the simulation in Case 1 is observed at $x_f \approx 1896$ m. The computed flow features evolve differently for each case as time progresses, leading to different stopping position depending on the cooling process.

Fig. 9 represents the evolution of temperature for the cases with heat exchange whereas Fig. 10 depicts the flow velocity at time $t = 100\,s$ for the three cases. When a cooling heat exchange is considered, i.e. Case 2 an Case 3, the fluid stops earlier due to the higher friction introduced by the change of viscosity and yield stress with temperature reduction.

In Fig. 11 the dependence between the basal stress τ_b and the depth-average temperature of the fluid column is shown. For both cases, linear model (Case 2) and piece-wise model (Case 3) profiles, the basal resistance increases as the temperature decreases, being higher in the cases of non-uniform temperature for most part of the temperature range. That is the reason why the flow in Case 3 stops earlier.

5.2. Test2: 1D flow over dry sloping bed

In this section a synthetic test case of 1D flow over a dry $S_0 = 0.033$ slope is considered. The fluid properties are described by the parameters in Table 4. This set of rheological parameters could be a plausible description for fluidized lava flow since they were estimated by observing the order of magnitude of the results presented in [12] for morphological observations in West Island. In the simulations, a constant flow of 2 m^3/s per unit width is assumed as inlet boundary condition with an initial temperature of 1500 K (left boundary section). Additionally, an air temperature of 300 K, convection coefficient $h_c = 50$ W/(m^2 K) and emissivity $\epsilon = 0.74$ are assumed.

Four different configurations will be compared, including uniform temperature profile (case M), piece-wise temperature profile with and without heat exchange with the bed (cases L1 and L2 respectively) and temperature diffusion profile (case D). Table 5 summarizes the main features of the models assessed in this test.

Table 6 includes the parameters resulting from the fitting of functions $f_1(\overline{T})$ and $f2(\overline{T})$ in (36) and (37) respectively for the piece-wise temperature and the temperature diffusion vertical profiles. The quality of the basal stress τ_b fitting to linear dimensionless relation (35) is measured using the relative root square error ($RRSE$) defined as:

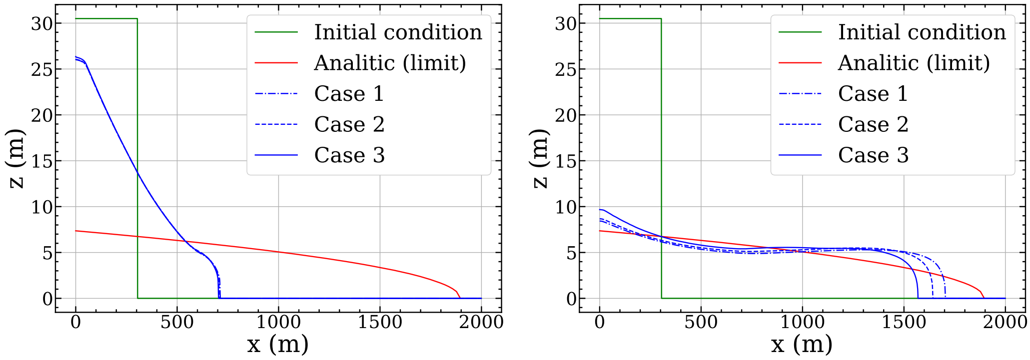

(a) t = 20 s (b) t = 100 s

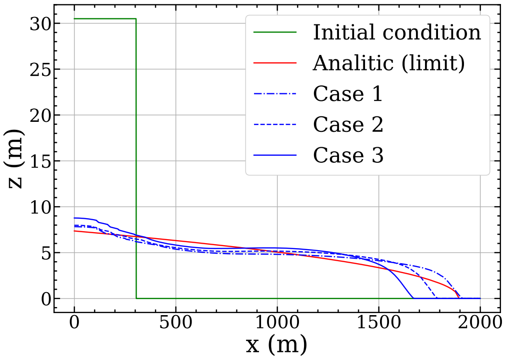

(c) t = 400 s

Fig. 8. Test 1. Free surface evolution for the different models.

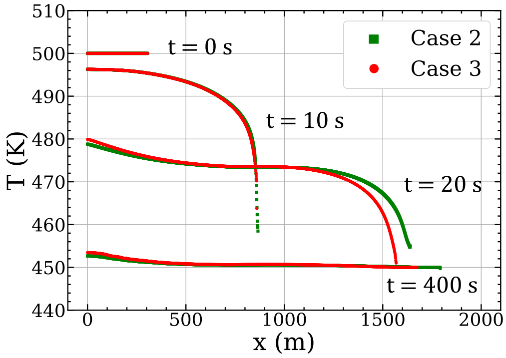

Fig. 9. Test1. Fluid temperature evolution.

Table 5
Test 2 - Configuration of the temperature profile.

Label	Temperature model	Bed heat conduction
M	Uniform	No
L1	Piece-wise	No
L2	Piece-wise	Yes
D	Diffusion	No

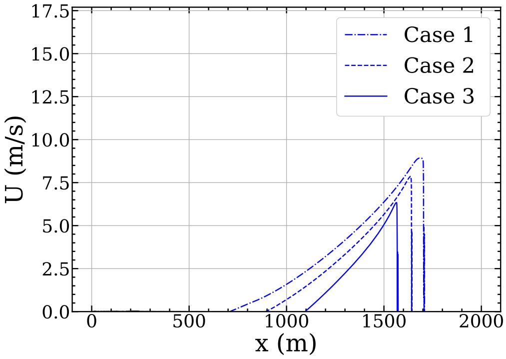

Fig. 10. Test1. Flow velocity at time $t = 100\,s$.

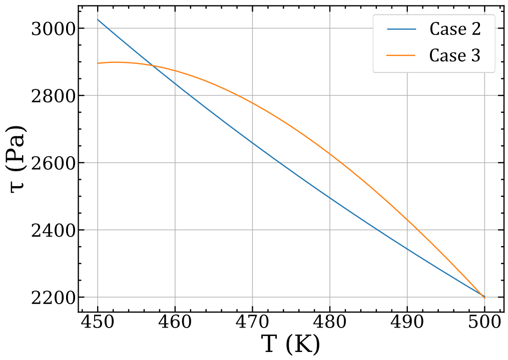

Fig. 11. Test 1 - Basal stress as a function of temperature in the case $\mathrm{U}/h = 1$.

Table 6
Test 2 - Fitting parameters of (36) y (37) (SI units).

	A_1	B_1	n_1	A_2	B_2	C_2	RRSE
Piece-wise	$1.38{\cdot}10^{-3}$	$1.88{\cdot}10^{-3}$	23.1	-18.1	22.6	-6.00	0.066
Diffusion	$-1.42{\cdot}10^{-3}$	$4.45\,{\cdot}10^{-3}$	3.03	3.61	-6.47	1.63	0.094

$$RRSE = \sqrt{\frac{\sum_{i=1}^{N}(\hat{\tau}_i - \tau_i)^2}{\sum_{i=1}^{N}(\overline{\tau} - \tau_i)^2}}, \tag{57}$$

where $\hat{\tau}_i$ are the predicted values for the basal stress from the fitted relations, τ_i are the exact values of the basal stress used as input to numerically compute the integral of velocity profile (26), following the procedure detailed in Section 3.2.1, and $\overline{\tau} = \sum_{i=1}^{N} \tau_i / N$ is the mean value.

Fig. 12 shows the basal shear stress τ_b depending on the depth-averaged temperature for each vertical temperature distribution considered. The basal stress is lower for both piece-wise temperature profiles, L1 and L2 respectively, and for the diffusion temperature profile M than for uniform temperature profile M. This difference reflects the fact that the interior of the fluid is hotter and hence has a lower viscosity and yield stress. It is worth mentioning that, for both linear piece-wise temperature profiles, L1 and L2 respectively, the basal shear stress is slightly higher than for the uniform temperature M when the average temperature is high ($T > 1400$ K). The explanation is that, while average temperature is still similar to that in the inner zone, the surfaces of the liquid cool significantly faster and they might cause a non-negligible increase in friction. Fig. 13 shows this effect, as simulations corresponding to configuration piece-wise L1 and piece-wise L2 move slower at the beginning and then overtake the one corresponding to the diffusion temperature configuration M.

Fig. 14 depicts the evolution of the flow depth along as the wave progresses downstream. We observe that the wavefront advances faster when a non-uniform temperature profile is used (L1, L2 and D) than with a uniform temperature M. These differences are even noticeable for the first stages after the dambreak. As the wave moves downstream, these differences increase remarkably.

In Fig. 15, the depth-averaged temperature along the dambreak flow is shown. Initially it is similar for all the configurations selected. However, as the dambreak wave progresses and the fluid becomes cooler, the configurations with non-uniform temperature profiles along the vertical coordinate have a lower heat transference as convection is computed considering the surface temperature.

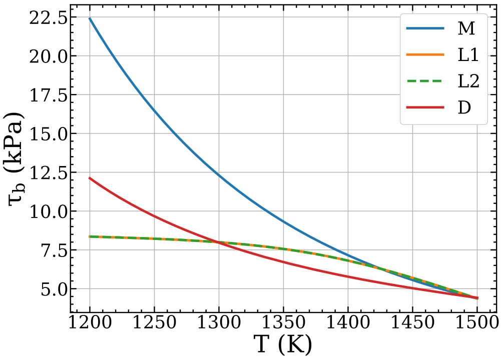

Fig. 12. Test 2. Basal stress as a function of temperature for U/$h = 1$.

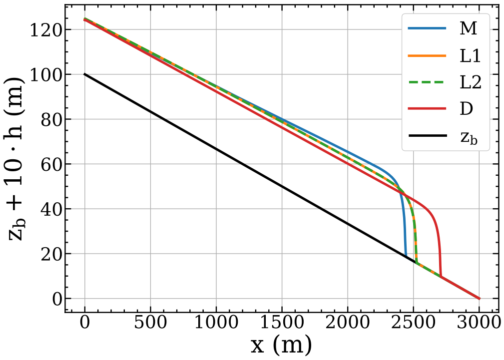

Fig. 13. Test 2 - Free surface representation ($z_b + 10h$) along the slope at t = 3450 s.

Table 7
Test 3 - Rheological parameters used for each model.

	A_τ (Pa)	B_τ (Pa)	C_τ (K^{-1})	A_μ (Pa· s)	B_μ (K)
Uniform	0	35·10^6	-0.01	0.05	9500
Linear	0	37·10^6	-0.01	0.02	9500
Piece-wise	0	37·10^6	-0.01	0.02	9500
Diffusion	0	37·10^6	-0.01	0.02	9500

Furthermore, cases piece-wise L1 and piece-wise L2 are almost indistinguishable, suggesting that conduction with the bed is negligible, which makes sense as it has a low thermal conductivity.

5.3. Test 3: experimental case of lava flow over 2D slope

A benchmark proposed in [42] for lava flow simulation models is now used for validation purposes. The test consists of a 2D sloping plane with $S_0 = 12,25°$. Over this plane, a constant flow of melted basalt $Q_{in} = 220\,mL/s$ at $T_{in} = 1050\,°C$ is poured. For its simulation, the values of emissivity and convection coefficient are the ones suggested in the reference publication: $\epsilon = 0.95$ and $h_c = 2$ W/(m^2· K), together with a density function $\rho(T) = 2350 - 0.01(T - 1073$ K) kg/m^3. The friction model is compared in the cases of uniform temperature profile, taken as reference, and the linear, the piece-wise and the diffusion temperature profiles. Viscosity and yield stress parameters are chosen independently for uniform temperature model and for the variable coefficients models, through a fitting process of the experimental data. The selected rheological parameters are presented in Table 7.

Fig. 16 displays the 2D map of depth-averaged temperature and flow depth at time $t = 42\,s$ for the piece-wise temperature profile. Note that the cooling process is faster for small depth zones.

Fig. 17-(a) depicts the evolution of the lava wave along the longitudinal section for the piece-wise temperature profile. Furthermore, Fig. 17-(b) shows a comparison between simulated and observed wavefront location for all the temperature distributions tested. The rheological parameters were set to obtain the best agreement between the computed wavefront location and the observed data. The coincidence between them is acceptable, although there is a discrepancy due to a change of the flow front velocity at $t = 20$ s approximately. This change could be explained due to irregularities in the experimental pouring. It is worth noting that, in the original work [42], all the considered models had the same discrepancy since the models were setup to fit observed data after that irregularity occurred.

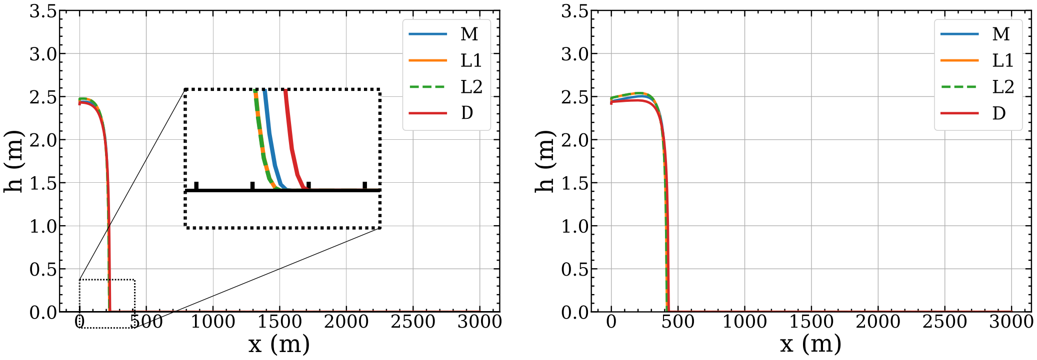

(a) t = 20 s

(b) t = 200 s

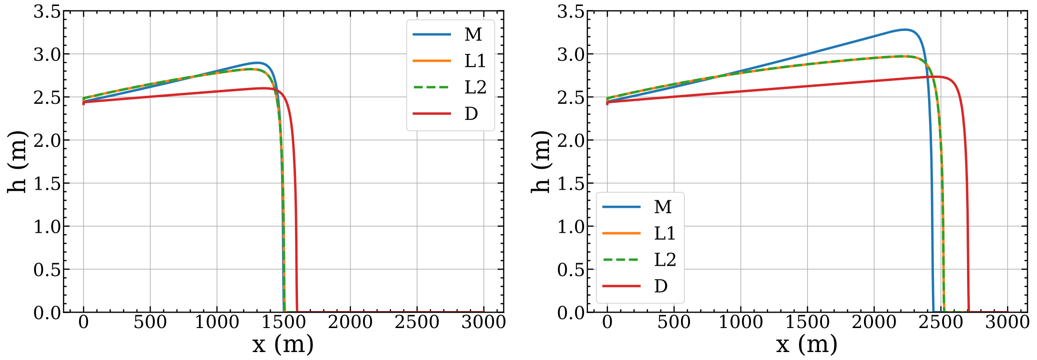

(c) t = 1950 s

(d) t = 3450 s

Fig. 14. Test 2 - Flow depth at t = 20 s, t = 200 s, t = 1950 s and t = 3450 s after the dambreak.

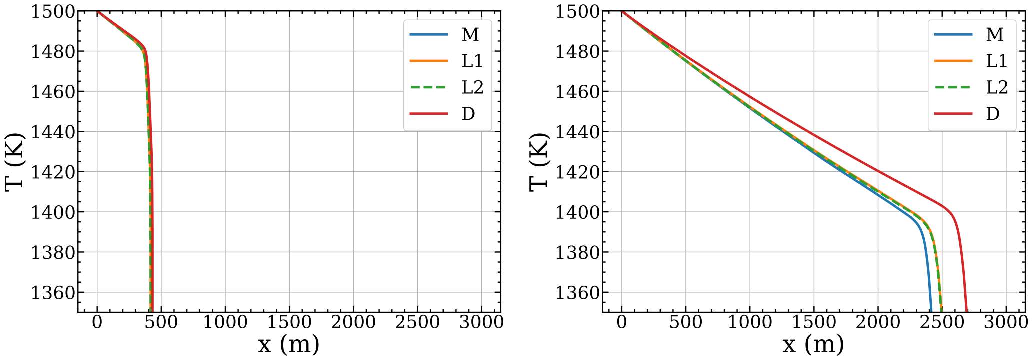

(a) t = 200 s

(b) t = 3450 s

Fig. 15. Test 2 - Depth-averaged temperature evolution along the dambreak at t = 200 s and t = 3450 s.

Finally, Fig. 18-(a) shows the comparison of the dambreak free surface at $t = 42\,s$ computed with all the temperature distributions tested. There exist differences between the piece-wise temperature profile and the other temperature distributions, including the classical uniform profile. These differences are clearly revealed when plotting the temporal evolution of the flow depth at $x = 50$ cm for all the temperature profile tested in Fig. 18-(b). The experimental values are higher than the simulation predictions, but the piece-wise temperature model is able to obtain slightly better approximation.

6. Conclusions

The present work is devoted to the formulation and numerical resolution of a new depth-averaged viscoplastic flow model with non-uniform temperature variation. A novel method has been developed and implemented to introduce the effects of a non-uniform vertical temperature profile on the depth-averaged flow equations. The proposed model has been discretized using a Finite Volume

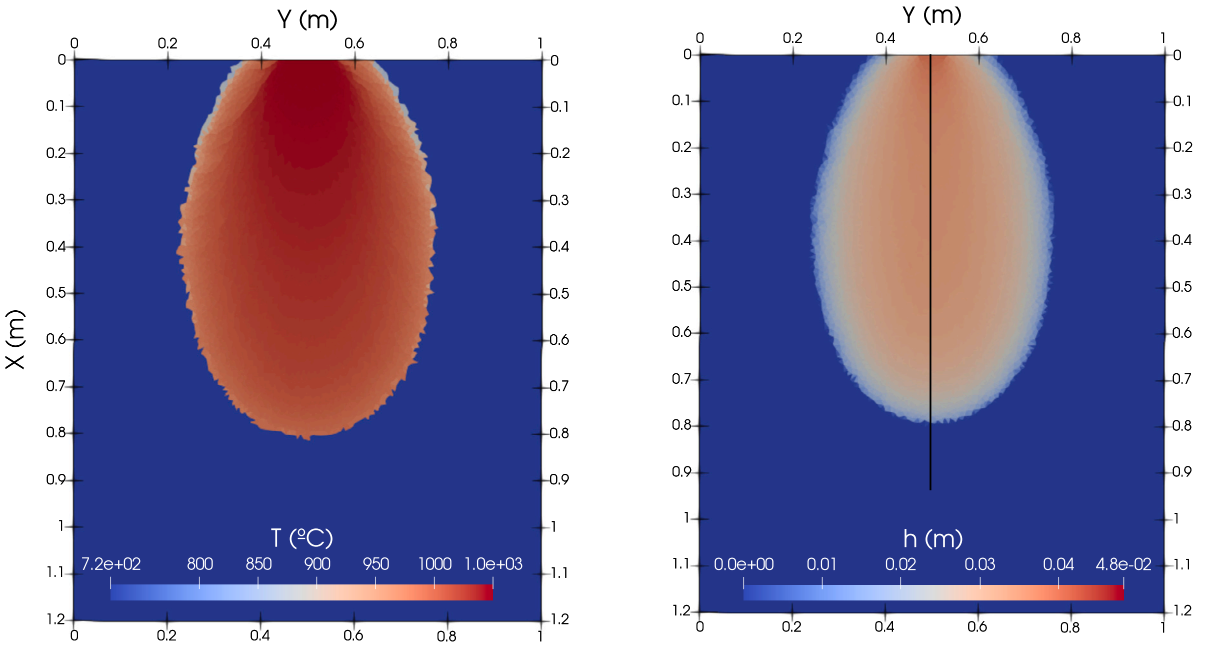

(a) Temperature

(b) Flow depth

Fig. 16. Test 3 - 2D maps of depth-averaged temperature and flow depth for the piece-wise temperature profile case at t = 42 s. (For interpretation of the colours in the figure(s), the reader is referred to the web version of this article.)

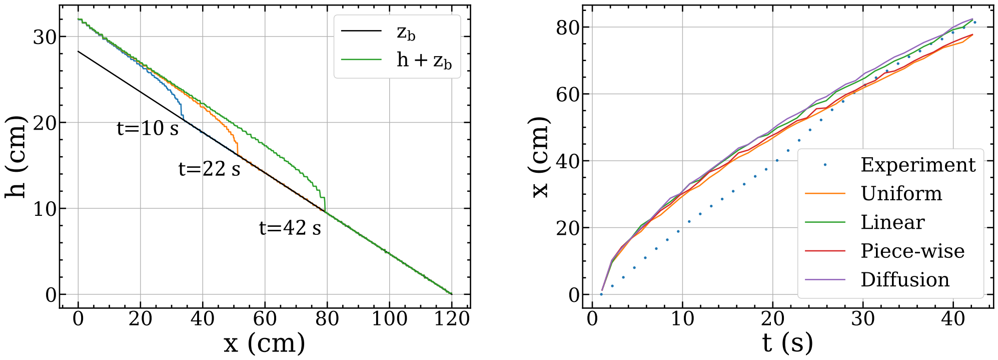

(a) Dambreak wave evolution for the piece-wise profile.

(b) Comparison between simulated and experimental wavefront location.

Fig. 17. Test 3 - Flow evolution along the central longitudinal section.

scheme recently shown to be useful for the efficient computation of unsteady thermally-driven shallow flows over steep topography and with complex rheology. Furthermore, the numerical algorithms are implemented for multi-CPU parallelization, decreasing hugely the computation time required to perform high-resolution simulations. This improves the parameter calibration process, makes longer simulations feasible and facilitates the study of the sensitivity with respect to the model parameters.

The novel non-uniform temperature model for the viscoplastic resistance has been tested in both 1D analytical and 2D experimental cases. From these benchmark tests it is concluded that the proposed non-uniform temperature profile modification undoubtedly has effects that can become very relevant in the bulk flow dynamics. It has been observed that, for low temperatures, a non-uniform temperature profile leads to lower friction contribution. This effect is explained because the inner layers of the flow column are hotter and hence more fluidized than under the uniform temperature hypothesis. For high temperatures, the behaviour depends on the parameters and profile assumed, being possible to have the reverse behaviour. The reason for this phenomenon is that the effects associated with rapid cooling of the upper and lower interfaces of the flow column can exceed the resistance of a flow with uniform high-temperature profile.

The results also suggest that, through a process of calibrating the parameters individualized for each model, the results can be very similar. This result suggests that use of uniform temperature models is subjected to a suitable calibration of the model parameters,

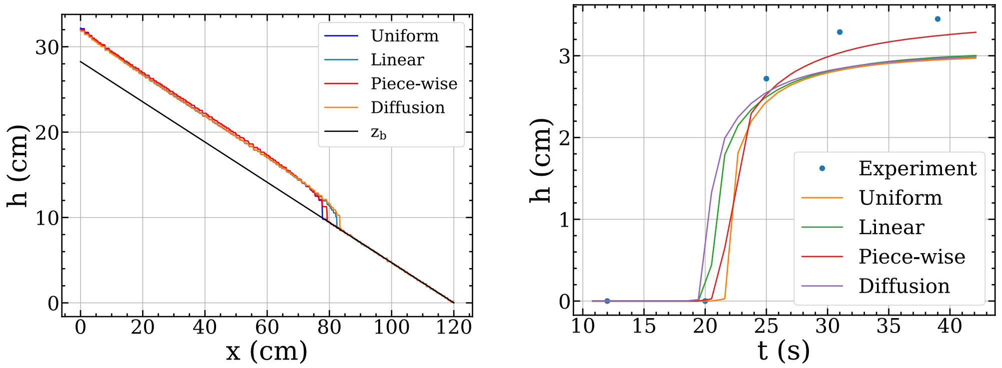

(a) Dambreak wave free surface at t=42 s.

(b) Comparison of the observed and computed flow depth evolution at $x = 50$ cm.

Fig. 18. Test 3 - Comparison of the observed and computed results along the central longitudinal section for uniform and linear temperature profile cases.

but it is necessary to conduct further tests to sustain the hypothesis. Finally, it has been determined that the effects of heat transfer by conduction at the bottom surface of the flow layer are negligible for the bulk flow dynamics, being sufficient to take into account radiation and convection heat transfer at the free surface.

CRediT authorship contribution statement

J. Ortega-Moya: Writing – review & editing, Writing – original draft, Visualization, Software, Methodology, Investigation, Formal analysis, Conceptualization. **S. Martínez-Aranda:** Writing – review & editing, Writing – original draft, Software, Conceptualization, Methodology. **J. Fernández-Pato:** Writing – review & editing, Writing – original draft, Software, Conceptualization. **P. García-Navarro:** Writing – review & editing, Writing – original draft, Supervision, Funding acquisition, Conceptualization.

Declaration of competing interest

The authors declare that they have no known competing financial interests or personal relationships that could have appeared to influence the work reported in this paper.

Data availability

Data will be made available on request.

Acknowledgements

This work was supported by project PID2022-137334NB-I00 funded by MCIN/AEI/10.13039/501100011033 and by ERDF/EU. The first author was funded by a “Degree Final Dissertation” student grant from the Aragón Institute of Engineering Research (I3A) - University of Zaragoza. This work has been partially funded by the Government of Aragón, through the research grant T32_23R Fluid Dynamics Technologies.

References

[1] S. Martínez-Aranda, J. Fernández-Pato, I. Echeverribar, A. Navas-Montilla, M. Morales-Hernández, P. Brufau, J. Murillo, P. García-Navarro, Volume models and Efficient Simulation Tools (EST) for Shallow flows, in: Advances in Fluid Mechanics: Modelling and Simulations, Springer, Singapore, 2022, pp. 67–137, Ch. Finite.
[2] O. Hungr, S. McDougall, Two numerical models for landslide dynamic analysis, Comput. Geosci. 35 (5) (2009) 978–992.
[3] W. Wu, Computational River Dynamics, NetLibrary, Inc, CRC Press, 2007.
[4] Z. Cao, Y. Li, Z. Yue, Multiple time scales of alluvial rivers carrying suspended sediment and their implications for mathematical modeling, Adv. Water Resour. 30 (4) (2007) 715–729.
[5] J. Fernández-Pato, S. Martínez-Aranda, P. García-Navarro, A 2D finite volume simulation tool to enable the assessment of combined hydrological and morphodynamical processes in mountain catchments, Adv. Water Resour. 141 (2020) 103617.
[6] E. Biagioli, M. de’ Michieli Vitturi, F.D. Benedetto, Modified shallow water model for viscous fluids and positivity preserving numerical approximation, Appl. Math. Model. 94 (2021) 482–505.
[7] I. Echeverribar, S. Martínez-Aranda, J. Fernández-Pato, R. García, P. Brufau, P. García-Navarro, A model for computing thermally-driven shallow flows, IOP Conf. Ser. Earth Environ. Sci. 1136 (1) (2023) 012037.
[8] A. Costa, G. Macedonio, Numerical simulation of lava flows based on depth-averaged equations, Geophys. Res. Lett. 32 (2005) L05304, https://doi.org/10.1029/2004GL021817.
[9] I. Echeverribar, S. Martínez-Aranda, J. Fernández-Pato, P. García-Navarro, A GPU-based 2D viscous flow model with variable density and heat exchange, Adv. Eng. Softw. 175 (2023) 103340.

[10] M.D. Thanh, The Riemann problem for the shallow water equations with horizontal temperature gradients, Appl. Math. Comput. 325 (2018) 159–178, https://doi.org/10.1016/j.amc.2017.12.031, https://www.sciencedirect.com/science/article/pii/S0096300317308901.

[11] M.R. Saleem, S. Zia, W. Ashraf, I. Ali, S. Qamar, The space–time CESE scheme for shallow water equations incorporating variable bottom topography and horizontal temperature gradients, Comput. Math. Appl. 75 (2018) 933–956, https://doi.org/10.1016/j.camwa.2017.10.021, https://www.sciencedirect.com/science/article/pii/S089812211730679X.

[12] M. Chevrel, T. Platz, E. Hauber, D. Baratoux, Y. Lavallée, D. Dingwell, Lava flow rheology: a comparison of morphological and petrological methods, Earth Planet. Sci. Lett. 384 (2013) 109–120.

[13] G. Hulme, The interpretation of lava flow morphology, Geophys. J. Int. 39 (2) (1974) 361–383.

[14] R.W. Griffiths, The dynamics of lava flows, Annu. Rev. Fluid Mech. 32 (1) (2000) 477–518.

[15] S. Martínez Aranda, Efficient Simulation Tools (EST) for sediment transport in geomorphological shallow flows, PhD Thesis, Universidad de Zaragoza, 2021.

[16] M. Dragoni, S. Pondrelli, A. Tallarico, Longitudinal deformation of a lava flow: the influence of Bingham rheology, J. Volcanol. Geotherm. Res. 52 (4) (1992) 247–254.

[17] M. Pastor, T. Blanc, B. Haddad, V. Drempetic, M.S. Morles, P. Dutto, M.M. Stickle, P. Mira, J.A.F. Merodo, Depth averaged models for fast landslide propagation: mathematical, rheological and numerical aspects, Arch. Comput. Methods Eng. 22 (1) (2015) 67–104.

[18] M. Jakob, O. Hungr, Debris-Flow Hazards and Related Phenomena, Springer Praxis Books, Springer, Berlin Heidelberg, 2005.

[19] S. Martínez-Aranda, J. Murillo, M. Morales-Hernández, P. García-Navarro, Novel discretization strategies for the 2D non-Newtonian resistance term in geophysical shallow flows, Eng. Geol. 302 (2022) 106625.

[20] M. Pastor, M. Quecedo, E. González, M.I. Herreros, J.A.F. Merodo, P. Mira, Simple approximation to bottom friction for Bingham fluid depth integrated models, J. Hydraul. Eng. 130 (2) (2004) 149–155.

[21] D. Naef, D. Rickenmann, P. Rutschmann, B.W. McArdell, Comparison of flow resistance relations for debris flows using a one-dimensional finite element simulation model, Nat. Hazards Earth Syst. Sci. 6 (1) (2006) 155–165, https://doi.org/10.5194/nhess-6-155-2006, https://nhess.copernicus.org/articles/6/155/2006/.

[22] W. Wittmann, F. Sigmundsson, S. Dumont, Y. Lavallée, Post-emplacement cooling and contraction of lava flows: InSAR observations and a thermal model for lava fields at Hekla volcano, Iceland, J. Geophys. Res., Solid Earth 122 (2017) 946–965, https://doi.org/10.1002/2016JB013444.

[23] M.R. Patrick, J. Dehn, K. Dean, Numerical modeling of lava flow cooling applied to the 1997 Okmok eruption: approach and analysis, J. Geophys. Res. 109 (2004), https://doi.org/10.1029/2003jb002537.

[24] P.Y. Burgi, M. Caillet, S. Haefeli, Field temperature measurements at Erta'ale lava lake, Ethiopia, Bull. Volcanol. 64 (2002) 472–485, https://doi.org/10.1007/s00445-002-0224-3.

[25] L. Keszthelyi, A.J. Harris, J. Dehn, Observations of the effect of wind on the cooling of active lava flows, Geophys. Res. Lett. 30 (2003), https://doi.org/10.1029/2003GL017994.

[26] O. Hungr, A model for the runout analysis of rapid flow slides, debris flows, and avalanches, Can. Geotech. J. 32 (4) (1995) 610–623.

[27] M. Pastor, M. Quecedo, J.A. Fernández Merodo, M.I. Herrores, E. González, P. Mira, Modelling tailings dams and mine waste dumps failures, Geotechnique 52 (8) (2002) 579–591.

[28] S. Martínez-Aranda, J. Fernández-Pato, P. García-Navarro, Mixing-phase model for shear-induced contractive/dilative effects in unsteady water-sediment mixture flows, Adv. Water Resour. 188 (2024) 104710.

[29] R.M. Iverson, D.L. George, A depth-averaged debris-flow model that includes the effects of evolving dilatancy. I. Physical basis, Proc. R. Soc. A, Math. Phys. Eng. Sci. 470 (2170) (2014) 20130819.

[30] M. Pastor, S. Tayyebi, M. Stickle, A. Yagüe, M. Molinos, P. Navas, D. Manzanal, A depth integrated, coupled, two-phase model for debris flow propagation, Acta Geotech. 16 (2021) 2409–2433.

[31] M. Quecedo, M. Pastor, M.I. Herreros, J.A. Fernández Merodo, Numerical modelling of the propagation of fast landslides using the finite element method, Int. J. Numer. Methods Eng. 59 (6) (2004) 755–794.

[32] M. Pastor, B. Haddad, G. Sorbino, S. Cuomo, V. Drempetic, A depth-integrated, coupled sph model for flow-like landslides and related phenomena, Int. J. Numer. Anal. Methods Geomech. 33 (2) (2009) 143–172.

[33] E.N. da Costa Andrade, A theory of the viscosity of liquids. Part II, Lond. Edinb. Dublin Philos. Mag. J. Sci. 17 (1934) 698–732, https://doi.org/10.1080/14786443409462427.

[34] C.V. Raman, A theory of the viscosity of liquids, Nature 111 (1923) 532–533.

[35] I.A. Abdelraziq, T.H. Nierat, Rheology properties of castor oil: temperature and shear rate-dependence of castor oil shear stress, J. Mater. Sci. Eng. 05 (2015), https://doi.org/10.4172/2169-0022.1000220.

[36] P. Kundu, I. Cohen, D. Dowling, Fluid Mechanics, Academic Press, 2015, https://books.google.es/books?id=uYevoQEACAAJ.

[37] J.B. Rawlings, Diffusion and Heat Transfer, University Lecture, 2014.

[38] R. Bird, W. Stewart, E. Lightfoot, Transport Phenomena, Transport Phenomena, Wiley, 2006.

[39] S. Martínez-Aranda, J. Murillo, P. García-Navarro, A robust two-dimensional model for highly sediment-laden unsteady flows of variable density over movable beds, J. Hydroinform. 22 (5) (2020) 1138–1160.

[40] J. Murillo, P. García-Navarro, Wave Riemann description of friction terms in unsteady shallow flows: application to water and mud/debris floods, J. Comput. Phys. 231 (2012) 1963–2001.

[41] S. Martínez-Aranda, J. Murillo, P. García-Navarro, A gpu-accelerated efficient simulation tool (est) for 2d variable-density mud/debris flows over non-uniform erodible beds, Eng. Geol. 296 (2021) 106462.

[42] H.R. Dietterich, E. Lev, J. Chen, J.A. Richardson, K.V. Cashman, Benchmarking computational fluid dynamics models of lava flow simulation for hazard assessment, forecasting, and risk management, J. Appl. Volcanol. 6 (2017) 9, https://doi.org/10.1186/s13617-017-0061-x.